Scientific Reports

https://doi.org/10.1038/s41598-026-38886-w

Article in Press

Bending behavior of concrete-filled FRP wound tubular arches with internal FRP bars

Received: 17 December 2025

Accepted: 31 January 2026

Published online: 09 February 2026

Cite this article as: Li B., Yang Z., Qi Y. *et al.* Bending behavior of concrete-filled FRP wound tubular arches with internal FRP bars. *Sci Rep* (2026). https://doi.org/10.1038/s41598-026-38886-w

Benben Li, Zhenyuan Yang, Yujun Qi, Zhenglong Zhou & Guowei Wang

We are providing an unedited version of this manuscript to give early access to its findings. Before final publication, the manuscript will undergo further editing. Please note there may be errors present which affect the content, and all legal disclaimers apply.

If this paper is publishing under a Transparent Peer Review model then Peer Review reports will publish with the final article.

ARTICLE IN PRESS

© The Author(s) 2026. **Open Access** This article is licensed under a Creative Commons Attribution-NonCommercial-NoDerivatives 4.0 International License, which permits any non-commercial use, sharing, distribution and reproduction in any medium or format, as long as you give appropriate credit to the original author(s) and the source, provide a link to the Creative Commons licence, and indicate if you modified the licensed material. You do not have permission under this licence to share adapted material derived from this article or parts of it. The images or other third party material in this article are included in the article's Creative Commons licence, unless indicated otherwise in a credit line to the material. If material is not included in the article's Creative Commons licence and your intended use is not permitted by statutory regulation or exceeds the permitted use, you will need to obtain permission directly from the copyright holder. To view a copy of this licence, visit http://creativecommons.org/licenses/by-nc-nd/4.0/.

Bending behavior of concrete-filled FRP wound tubular arches with internal FRP bars

Benben Li[a], Zhenyuan Yang[a], Yujun Qi[a,*], Zhenglong Zhou[a], Guowei Wang[b]

[a] College of Civil Engineering, Nanjing Tech University, Nanjing 211816, China

[b] Bengbu Expressway Management Center of Anhui Transportation Holding Group Co., Ltd., Bengbu 233040, China

*Corresponding author: qiyujun11@126.com(Yujun Qi)

Abstract：Conventional reinforced concrete arches are susceptible to corrosion in underground environments, leading to reduced durability. This study proposes concrete-filled FRP (Fiber-reinforced polymer) wound tubular arches with internal FRP bars to achieve excellent corrosion resistance. Eighteen concrete-filled FRP tubular arches were tested under mid-span concentrated loading, and the effects of FRP tube wall thickness and FRP reinforcement configuration were investigated. The experimental results demonstrate that increasing the wall thickness of the FRP tube significantly enhances the ultimate load-bearing capacity, with a maximum increase of 104.7%

observed under mid-span loading. The incorporation of FRP reinforcement also resulted in 236.3%~279% increase of ultimate capacity and 111.11%-119.67% increase of displacement ductility ratio. A simplified theoretical model for predicting the ultimate load of concrete-filled FRP tubular arches with internal FRP bars was proposed, achieving a relative error within 10%. The proposed concrete-filled FRP tubular arch demonstrates considerable potential for application in underground engineering.

Keywords GFRP tubular arches, GFRP rebar, Ultimate load, Bending behavior

Introduction

Arch structures are widely used in underground engineering support and reinforcement systems due to their excellent load-bearing capacity and rational force transmission mechanism. However, underground environments are typically harsh, characterized by darkness, high humidity, and acidic media, which can cause concrete deterioration, leading to structural loosening and significant strength degradation[1]. Additionally, complex subsurface stress conditions, including geostatic pressure, groundwater pressure, and seismic forces, can induce deformation and damage in arch structures[2–4].

Concrete-filled fiber-reinforced polymer (FRP) tube arches (referred to as CFFT arches) represent an emerging structural form with promising potential in corrosion-prone engineering applications such as bridges and culverts. Although research on straight FRP tube-confined concrete members is relatively mature[5,6], recent study has revealed that even such straight members can exhibit complex stress reduction-recovery responses, attributable to factors including concrete core brittleness, shrinkage, non-uniform confinement from sectional geometry, insufficient confinement from FRP materials, and internal arching action[7]. Given this complexity, the industrial fabrication of curved FRP tubes presents additional challenging, and studies on curved FRP tube-confined concrete arch structures are remain limited[8]. Beyond CFFT arches, FRP sheets have also been explored as flexible membranes to connect concrete voussoirs in prefabricated arch bridges, with performance heavily reliant on FRP-concrete bond quality and reinforcement layout[9]. Dagher et al.[10] investigated the flexural behavior of CFFT arches through quasi-static tests and fatigue failure tests after two million fatigue cycles. The results showed consistent mid-span load–deflection responses and validated the linear strain distribution assumption. Majeed [11] tested scaled CFFT short-span arch bridges under backfill and field loading. A beam-based finite element model successfully predicted load capacity, deformation, strain response, ductility, and failure modes (FRP rupture or concrete crushing).

CFFT arch structures show promise not only in bridge and culvert applications but also in underground protective engineering. For example, Wang et al.[12] fabricated CFRP tube arches using a hand lay-up process and conducted blast tests. The structures maintained considerable integrity and load-bearing capacity after explosions, demonstrating excellent blast resistance. Liu’s team[13] further tested CFRP circular arches under varying blast conditions. The CFRP shell’s circumferential confinement was found to significantly enhance the concrete's resistance to shear and splitting, increasing the peak load and extending the deformation plateau. However, under extreme blast loads, the failure modes included CFRP ablation and concrete pier damage. Dong et al.[14,15] studied the ultimate bearing capacity of BFRP tube arches, particularly under combined bending–shear failure. Arches with different curvature radii showed varying capacity improvements, with the 150° radius providing the most significant enhancement. Wei[16] investigated the mechanical performance of concrete-filled steel tubular (CFST) arch bridges in corrosive environments (hygrothermal, saline-alkali, and marine conditions). Parametric analysis indicated that the in-plane bearing capacity under mid-span concentrated load increased with the number of FRP layers, rise-to-span ratio, and steel ratio, but decreased with the slenderness ratio. Burnton et al.[17] developed a full-scale prototype of a novel hybrid double-skin tube arch (DSTA) bridge, comprising DST beams, columns, and arches. Connections were achieved by welding steel tubes and bonding FRP tubes using prepreg or wet lay-up techniques. Fernando et al.[18] conducted a parametric study on DSTA arches, considering FRP tube thickness, steel tube position (concentric/eccentric), and loading configurations. The results showed that DSTA arches possess significantly higher load-bearing capacity and ductility than equivalent reinforced concrete arches. The concentric steel tube configuration performed optimally under moment reversals along the arch axis. Numerical models accurately predicted DSTA behavior up to the ultimate load; post-peak degradation was attributed to shear connector failure at the steel–concrete interface.

In summary, existing research on FRP tube arches has primarily relied on manual fabrication (e.g., hand lay-up) for shaped tubes, limiting consistency, production efficiency, and structural reliability. Furthermore, studies have predominantly focused on high-cost CFRP materials. In contrast, this study introduces a novel, fully automated filament-winding manufacturing process for producing pre-curved GFRP arch tubes. This technological advancement represents a significant departure from conventional methods by enabling precise, repeatable, and industrialized fabrication of complex curved composite sections. Leveraging the economic and corrosion-resistant advantages of GFRP, the proposed member—a concrete-filled filament-wound GFRP tube internally reinforced with FRP bars—offers a viable and efficient composite solution, thereby addressing a gap in both manufacturing technology and structural application for GFRP arches. Its design allows for seamless integration with common support systems in underground engineering (e.g., combined with rock bolts and shotcrete for tunnel support) and potential applications in bridge engineering. The mechanical behavior and failure modes of this new arch system under mid-span loading are systematically investigated and a corresponding analytical model for predicting its ultimate bearing capacity is developed.

Experimental program

Manufacturing technology

The GFRP arches utilized in this experiment were manufactured by Shandong Xinjierui Composite Materials

Technology Co. Ltd., with three nominal wall thicknesses: 3 mm, 5 mm, and 7 mm. An automatic GFRP arch winding device was developed to achieve the mechanized production of GFRP arches (Fig.1). After the fibers were immersed in resin tank, they were pulled and wound around the integral solid winding core to form GFRP arches. After the resin was solidified, the specimens were demolded with specially designed demolding equipment for GFRP arches. The dimension of the arches is shown Fig.2. The bending radius of the GFRP arch at the centroid of the cross-section was 650 mm, and the bending angle was 90°. The internal cross-sectional diameter of the GFRP tube was 50 mm. Based on these dimensions, the span of the arch was 920mm, the rise was 190mm, and the rise-to-span ratio was 0.206.

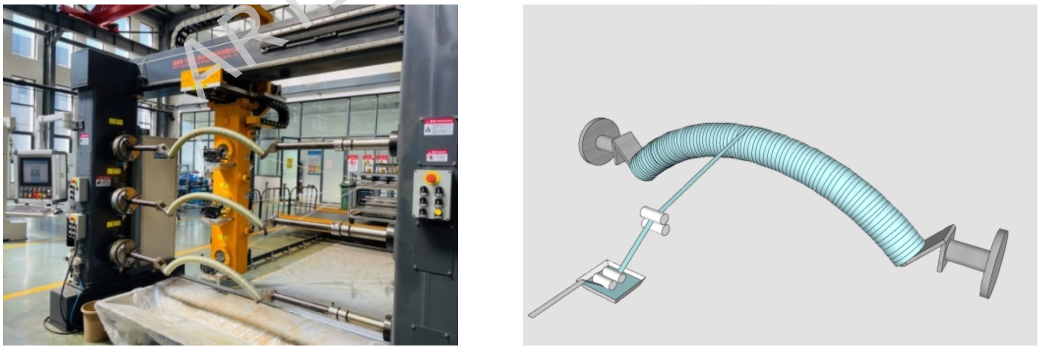

(a) Automatic GFRP arch winding device (b) Winding process of GFRP arches

Fig. 1. Manufacturing process of GFRP arches

(a) Hollow FRP tubular arches (b) Concrete-filled FRP tubular arches

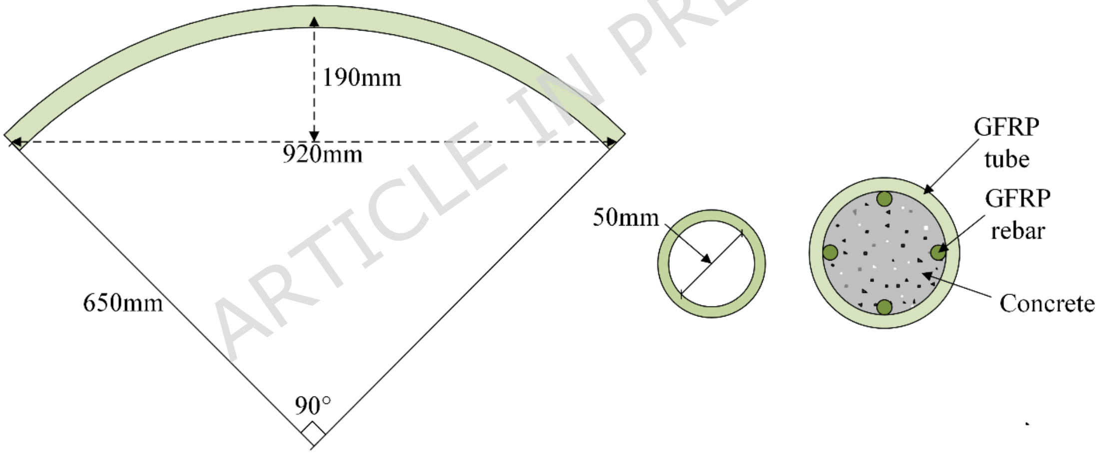

(c) Basic parameters of GFRP tubular arch and arch section

Fig.2. Preparation of concrete-filled FRP tubular arches

Material properties

The filament-wound GFRP tubes used in the tests were wound at 85°, which was nearly hoop-oriented. Following the ASTM

D2290-12 (2012)[19], the “split-disk” method was used to test the hoop tensile properties of GFRP arches. The hoop ultimate tensile strength, hoop ultimate tensile strain, and mean hoop tensile modulus of the GFRP pipes are summarized in Table 1[20]. It should be noted that the observed trend of decreasing hoop tensile strength with increasing tube thickness, as shown in Table 1, is primarily attributed not to manufacturing variability or material anisotropy, as all specimens were fabricated using identical processes. Instead, this phenomenon stems from an inherent systematic limitation of the ASTM D2290 split-disk method itself. This method measures an ‘apparent’ hoop tensile strength under a combined tensile-bending stress state. In thicker-walled specimens, significant local compressive and shear stresses can trigger failure modes such as local crushing or delamination, rather than the ideal tensile fracture of fibers. This leads to a lower measured failure load. Recent research[21] indicates that using modified ring specimens can yield values closer to the material's intrinsic strength. The data trend herein validates this geometric dependency of the standard method, reflecting a ‘structural’ response under a specific test condition, which is crucial for accurate material performance interpretation.

The axial ultimate compressive strength, axial ultimate compressive strain, and mean axial compressive modulus were determined in accordance with the Chinese standard GB/T 1448-2005[22] "Fiber-Reinforced Plastics—Determination of Compressive Properties" part, the results are also provided in Table 1. It is noted that the GFRP tube showed a relatively low axial compressive modulus due to the nearly hoop-oriented fibers. Cement-based grouting concrete rather than conventional concrete was used in the tests because the internal diameter of the GFRP tube is only 50 mm. The coarse aggregates in ordinary concrete could affect the compactness inside the tube and potentially create voids. The compressive strength tests of the concrete specimens were conducted following the Chinese standard GB/T 50081-2019[23]. The mean compressive strength of the grout was measured to be 40.7 MPa. The GFRP rebars used as longitudinal reinforcement were commercially available straight bars with a diameter of 4 mm, supplied by Jiangsu Fibre New Material Technology Co., Ltd. They were composed of E-glass fibers within an epoxy resin matrix, with a fiber volume fraction of approximately 66%-68%. Based on the manufacturer's certification, the tensile strength was 1035 MPa, and the elastic modulus was ≥ 50 GPa.

Table 1. Material property test results of FRP tube

Thickness (mm)	Hoop Tensile			Axial Compression		
	Strength (MPa)	Fracture Strain	Modulus (GPa)	Strength (MPa)	Fracture Strain	Modulus (GPa)
3	794.57	0.0117	18.13	119.12	0.0097	10.457
5	566.14	0.0120	12.32	169.23	0.0161	15.846
7	560.08	0.0133	11.81	188.35	0.016	17.579

Arch Specimen design

To study the failure mechanism of concrete-filled FRP tubular arches, a single point loading test at the mid span of composite arch was designed. The experimental program involved 18 arch specimens where two identical specimens were prepared in one group. The preliminary design of the specimens is shown in Table 2. Specimen labeling adheres to this convention: "A" designates arch specimens; "T+3/5/7" indicates GFRP tube thicknesses of 3mm, 5mm, or 7mm; "E" denotes empty tube specimens; "F+0/4" represents tubes filled with C40 grout containing zero or four embedded FRP bars; "C" corresponds to mid-span loading configurations. The configuration of four embedded FRP bars can be found in Fig.2(c). Due to their inherent flexibility, the rebars were easily placed inside the GFRP tube arch during assembly without requiring any thermal-forming. After FRP bars were embedded in the hollow GFRP arches, grouting concrete were casted to form the composite arches.

Test setup

The single-point mid-span loading test on the concrete-filled FRP tubular arch was performed using a 500-ton universal testing machine. The single-point mid-span loading scheme was adopted to induce a critical and clearly identifiable bending condition at the crown, facilitating a fundamental assessment of the arch's flexural capacity. A detailed discussion on the implications of this loading condition is provided in “Considerations on loading scheme”Section. The Test apparatus is shown in Fig.3(a). A curved loading head fitted with a rubber pad was attached to the actuator to match the arch crown’s geometry. To mitigate stress concentration and prevent localized failure, the arch ends were reinforced with carbon fiber sheets and steel clamps. Lateral supports were installed on both sides to restrain possible large out-of-plane deformation. In the experiment, fixed supports (Fig. 3b) were installed at the arch ends. The inclined surface of each support matched the cross-section of the arch end. The arch end movement was restrained by a ring-shaped steel block, and wooden wedges were inserted into the gaps to prevent any displacement or rotation. Three vertical displacement transducers were placed below the mid-span and both quarter-span points. As shown in Fig. 3(c), sixteen strain gauges were bonded at eight locations—each with a pair of perpendicular gauges measuring hoop and longitudinal strains. These included the mid-span (side and bottom), left and right quarter-span points (crown, side and bottom). No strain gauges were installed at the mid-span crown due to direct loading. The strain gauges of the arch specimen were numbered as shown in Fig. 3(d), with odd numbers indicating circumferential strain gauges and even numbers indicating longitudinal strain gauges. The loaded was applied under displacement control at a rate of 0.5 mm/min.

Table 2. Design parameters of the specimens

Specimen Number	Thickness (mm)	Filler	Ultimate capacity (kN)	Δ_u (mm)	Δ_y (mm)	μ	E (kN·mm)
AT3EC	3	-	8.46	12.44	10.63	1.17	39.37
AT3F0C		C40 concrete	14.96	9.42	7.45	1.26	69.77
AT3F4C		C40 concrete +4×4mm FRP rebar	32.06	36.16	14.65	2.47	714.32
AT5EC	5	-	13.50	15.76	12.97	1.22	90.78
AT5F0C		C40 concrete	21.96	15.89	9.58	1.65	196.48
AT5F4C		C40 concrete +4×4mm FRP rebar	43.19	32.73	12.19	2.68	855.71
AT7EC	7	-	17.32	15.36	11.57	1.33	145.67
AT7F0C		C40 concrete	19.80[a]	8.75	7.06	1.24	80.63
AT7F4C		C40 concrete +4×4mm FRP rebar	58.25	36.57	13.01	2.81	1205.62

Note: [a] Early failure due to out of plane displacement of the specimen.

(a) Test apparatus

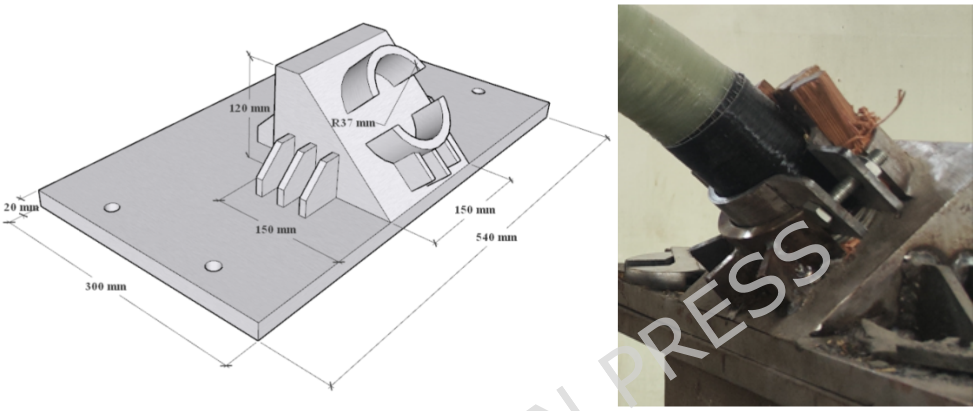

(b) Details of the supports

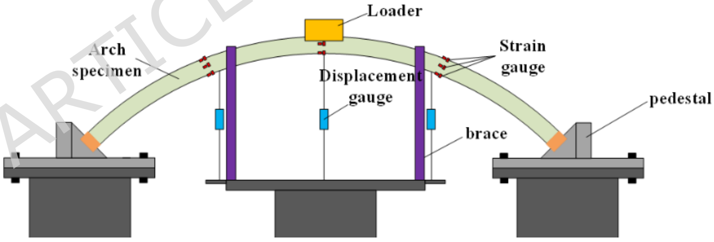

(c) Arrangement of strain gauges and displacement sensors

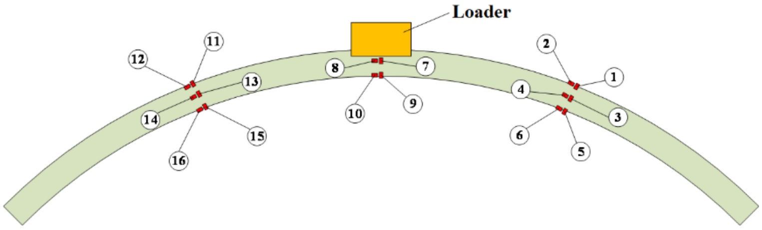

(d) Strain gauge number

Fig.3. The single-point mid-span loading testing

Test results and discussion

Considerations on loading scheme

In practice, underground arches are subjected to distributed loads, with the most critical loading positions for conventional arches typically at the one-third or one-quarter span points. This study employed a single-point mid-span loading scheme to investigate the fundamental mechanical performance of the novel GFRP-concrete composite arch. This choice was based on the following considerations.

Firstly, a concentrated load at the crown induces the maximum bending moment at a single, well-defined section, creating a critical condition for evaluating the arch’s flexural capacity. Secondly, this setup is designed to probe the internal force redistribution capability of the statically indeterminate system by inducing a clear failure sequence—initiating with a plastic hinge at the crown, potentially followed by hinge formation at other sections like the quarter points. This process is crucial for understanding the systemic collapse mechanism. Loading directly at a traditional critical position might lead to premature local failure, hindering observation of this global behavior. Finally, this simplified scheme establishes a clear performance benchmark, essential for isolating the effects of load distribution in future studies involving more realistic distributed loads.

Regarding the nature of this loading condition, the mid-span point load is critical for the ultimate flexural capacity of the crown section, as it maximizes the bending stress at that point. However, for overall system behavior involving multi-hinge mechanisms, distributed loading may lead to a different, potentially more critical, failure mode. A qualitative comparison highlights the practical implications. A mid-span point load produces a highly localized peak moment, leading to a failure governed by the flexural strength of the crown section. In contrast, a uniformly distributed load results in a more uniform moment distribution, often promoting a progressive collapse with hinges forming at multiple locations, which engages higher system redundancy. Therefore, the adopted loading scheme provides a fundamental test and a performance benchmark. The structural response under practical distributed loads remains a vital consideration, and investigating such performance is a logical next step, for which this work serves as a foundation.

Failure modes

The failure modes of specimens with different variables (GFRP arch wall thickness and FRP reinforcement configuration) are shown in Fig. 4.

Fig. 4(a) illustrates the failure patterns of specimens AT3EC, AT5EC, and AT7EC. During the initial loading stage, the load and displacement increased linearly, indicating that the FRP arch was in the elastic phase. For specimens AT3EC and AT5EC, upon reaching the ultimate load, audible cracking sounds accompanied fiber fracture, and fine cracks appeared near the mid-span bottom of the GFRP arch. Subsequently, the load dropped, and the specimens lost load-bearing capacity. For specimen AT7EC, after initial cracking at the mid-span, loading continued until another crack developed near the crown of the right quarter-span point. This crack propagated rapidly, leading to the loss of load-carrying capacity.

Fig. 4(b) depicts the failure modes of specimens AT3F0C, AT5F0C, and AT7F0C, which were fabricated by filling the GFRP arches with only concrete. During the initial loading phase, the load increased linearly with displacement at a rapid rate, indicating that both the FRP arch and the core concrete were in the elastic stage. At a certain point, a dull “pop” sound indicative of resin cracking was heard, and a whitening mark appeared on the surface of the FRP arch near the mid-span bottom. As the load continued to increase, the whitened area widened and developed into a crack, accompanied by intermittent fiber fracture sounds. Subsequently, cracks emerged randomly near the crown regions of both the left and right quarter-span points. Under further loading, these cracks at the quarter-span point crowns propagated, while fracture at the mid-span bottom became increasingly evident.

Fig. 4(c) shows the failure modes of specimens AT3F4C, AT5F4C, and AT7F4C, which were prepared with C40 grout and embedded with FRP reinforcement inside the GFRP elbow tubes. In the initial elastic stage, the load–displacement response exhibited a linear increase, similar to that of the specimens without FRP reinforcement. At a certain load level, a crack formed near the mid-span bottom of the composite tube, accompanied by a slight drop in the load. With continued loading, the load resumed increasing until cracks appeared randomly near the crown of the left and/or right quarter-span points. As loading proceeded, these cracks widened progressively, and fracture at the mid-span bottom became more pronounced. It is noted that no displacement or rotation was observed at the ends of the arch specimen during the experiment.

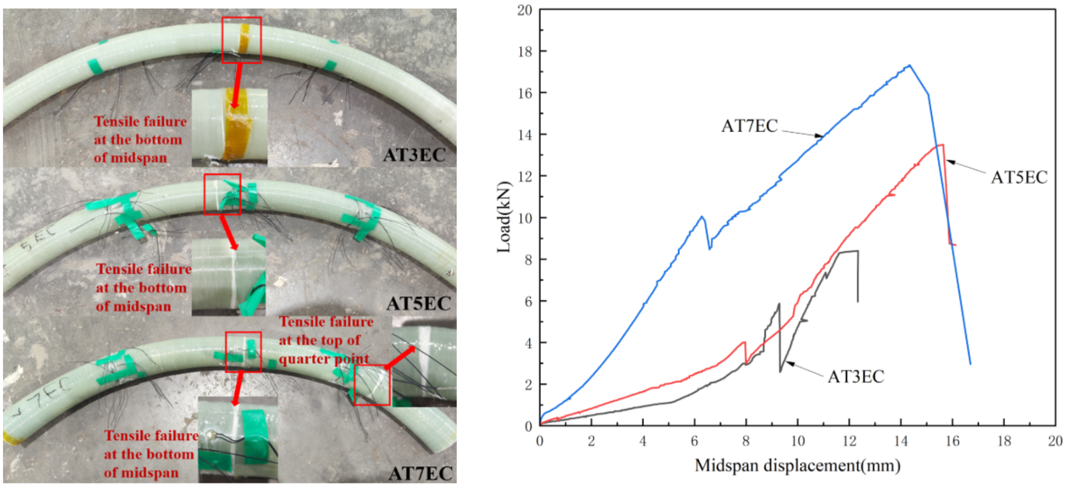

(a) Hollow GFRP arch

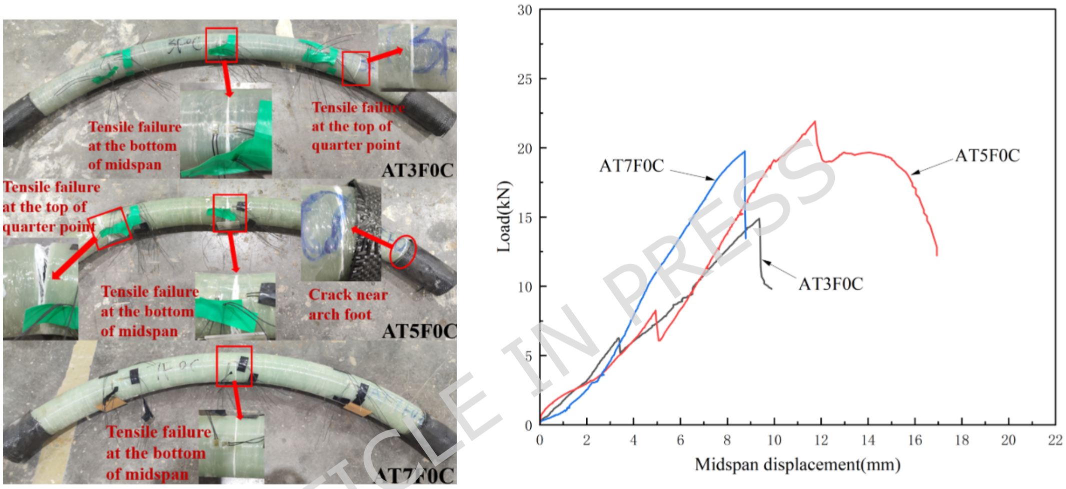

(b) Concrete-filled GFRP arch without FRP bars

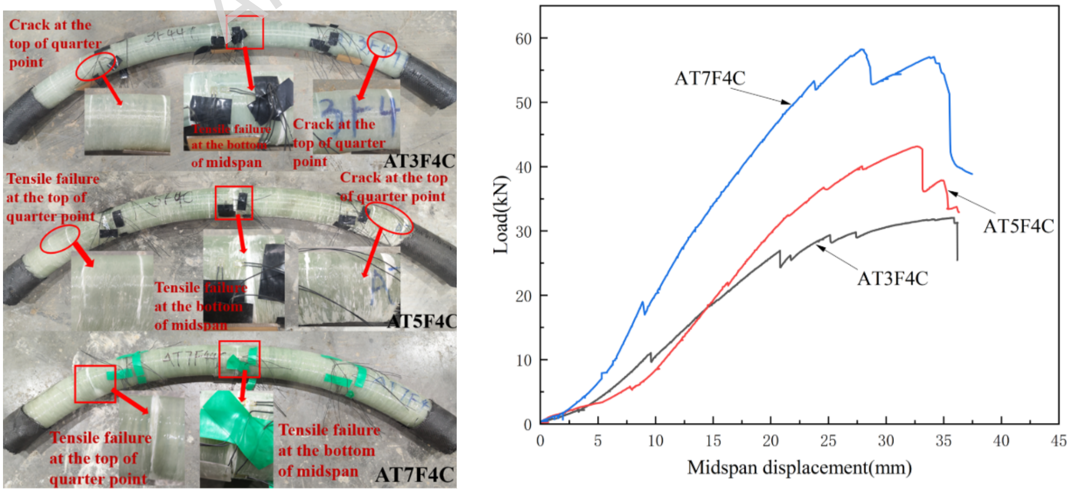

(c) Concrete-filled GFRP arch with internal FRP bars

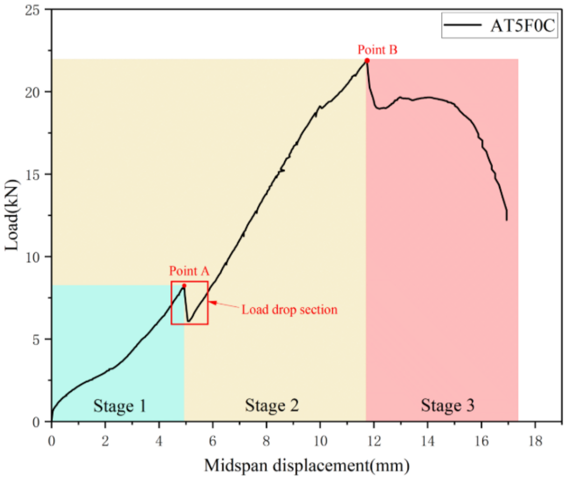

(d) Typical load-displacement curve of GFRP tubular arch

Fig.4. Failure modes and load-displacement curve of specimens

Load -displacement curves and ultimate load-bearing capacity

The load-midspan displacement curves are shown in Fig.4. These curves indicate that concrete-filled GFRP arches exhibit similar responses during mid-span loading. Using specimen AT5F0C as an example, the typical load-midspan displacement curve (Fig.4(d)) is characterized by three distinct phases. Initially, the arch exhibits elastic behavior with rapid load increase and slow displacement growth, showing an approximately linear relationship. The initial stiffness (ascending slope) varies with GFRP tube thickness, where a thicker tube provides stronger hoop confinement, enhancing the concrete's compressive response and thus increasing the composite section's initial axial and flexural stiffness. Upon reaching Point A, the specimen enters Stage 2, marked by a minor load drop. This is primarily due to resin matrix cracking in the GFRP tube at the mid-span bottom. Subsequent loading shows a flattened curve with intermittent load drops, as the GFRP tube carries longitudinal tensile stresses under combined compression-bending in segments near the fracture. This phase represents the formation and development of plastic hinge regions, where the confinement from the GFRP tube crucially enhances the concrete's compressive ductility, allowing the hinge to sustain moment under large rotation and facilitating internal force redistribution. Cracking on the tensile side primarily involves the failure of the matrix and potential local fiber debonding, which compromises longitudinal load transfer and partially disrupts hoop continuity in that specific region. However, in the compression zone of the arch, the concrete is in a favorable state of triaxial compression. The GFRP tube, with its fibers oriented at 85° (primarily in the hoop direction), remains largely intact and well-bonded to the concrete. Here, the concrete still attempts to expand laterally under axial compression, and the GFRP tube, by virtue of its dominant hoop fibers, continues to provide effective confinement. Furthermore, the global load path remains intact. The arch functions as an integral unit where load is transferred via axial compression and bending moment. Even after the formation of a plastic hinge at mid-span, significant axial force continues to flow through the entire cross-section, including the compression zone. This substantial axial compression is the fundamental driver for the lateral expansion of the concrete, thereby activating the hoop confinement provided by the GFRP tube. Thus, while cracking alters the moment distribution, it does not eliminate the critical axial force that engages the confinement mechanism. At Point B, tensile cracks form near quarter-span point crowns as the GFRP arch reaches tensile strength, leading to rapid displacement growth. Ultimately, structural failure and loss of bearing capacity resulted from excessive crack propagation. The ultimate failure was characterized by tensile fracture of the GFRP tube fibers in high-tension regions (e.g., the mid-span bottom and quarter-span tops), accompanied by audible cracking sounds. In contrast, the concrete in compression zones remained uncrushed, with the tube showing signs of whitening. This tensile-controlled failure mode confirms that effective confinement shifts the structural weak link to the tension side.

The ultimate load-bearing capacities of specimens can be found in Table 2. Compared to specimen AT3EC, the ultimate load-bearing capacities of specimens AT5EC and AT7EC increased by 59.5% and 104.7%, respectively. Similarly, compared to specimen AT3F0C, the ultimate capacities of AT5F0C and AT7F0C increased by 46.8% and 32.4%, respectively. When compared to AT3F4C, specimens AT5F4C and AT7F4C exhibited increases of 34.7% and 81.7% in ultimate load capacity, respectively. Clearly, the ultimate load-bearing capacity improved with increasing wall thickness of the composite tube. By examining the trends of the load–displacement curves of specimens with different wall thicknesses in Fig.4, it can be observed that thicker tube walls result in a steeper slope during the elastic phase, indicating higher structural stiffness.

The influence of internal FRP reinforcement can also be found in Table 2. The results indicate that compared to specimen AT3EC, the ultimate load capacities of AT3F0C and AT3F4C increased by 76.8% and 279%, respectively. Relative to specimen AT5EC, specimens AT5F0C and AT5F4C showed enhancements of 62.7% and 242.1%, respectively. In comparison with AT7EC, the ultimate capacities of AT7F0C and AT7F4C were raised by 14.3% and 236.3%, respectively.

For each concrete-filled FRP arch with internal FRP bars, the contribution rate of each component (GFRP hollow elbow tube, C40 concrete and GFRP bars) to the ultimate load-bearing capacity is calculated. For specimen AT3F4C, the contribution rates of GFRP hollow elbow tube, C40 concrete and GFRP bars are 26%, 20% and 53%, respectively; for specimen AT5F4C, they are 31%, 20% and 49%. This establishes a clear trend: the concrete core provides a stable proportional contribution of approximately 20%, while the internal FRP bars are the dominant component, contributing about 49%–53% of the total capacity. For the specimen with the thickest tube (AT7F4C), the contribution of the GFRP tube is directly measured as 30%. However, due to the early out-of-plane failure of the reference specimen AT7F0C (without FRP bars), the concrete contribution for this series cannot be obtained directly. To ensure a reliable analysis, the concrete contribution for AT7F4C is inferred based on the consistent ~20% trend observed in the 3mm and 5mm tube specimens, which is supported by the mechanism of enhanced concrete confinement with increasing tube thickness. Consequently, the contribution of the internal GFRP bars in AT7F4C is derived by subtracting the tube contribution and this inferred concrete share from the total capacity, yielding a value around 50%, which aligns seamlessly with the established trend. Therefore, although the precise values for the AT7F4C specimen carry a slightly higher uncertainty, the key conclusions of the study remain robust and are in fact reinforced by this logical inference. The direct measurements from the 3mm and 5mm tube specimens conclusively demonstrate that the FRP bars are indispensable, providing approximately half of the ultimate load-bearing capacity despite occupying only about 2% of the cross-sectional area..

Ductility analysis

To quantitatively assess the influence of different structural parameters on ductility, the displacement ductility ratio (μ) and the energy absorption capacity (E) are adopted as key metrics. The displacement ductility ratio μ is calculated as the ratio of ultimate displacement Δ_u (the ultimate displacement corresponding to a 20% drop in the peak load) to equivalent yield displacement Δ_Y (determined using the equivalent energy method). This reflects the deformation capacity prior to failure. The energy absorption capacity E is calculated as the area under the load–displacement curve from the onset of loading to the ultimate displacement Δ_u, representing the total energy dissipated before failure.

The calculated ductility indices for all specimens can be found in Table 2. Compared to the hollow GFRP tube specimens, the concrete-filled specimens (AT3F0C and AT5F0C) exhibited an increase in energy absorption capacity by 77% to 116% and an improvement in displacement ductility ratio by 8% to 35%. This indicates that concrete filling effectively enhances the energy dissipation capacity and, to a certain extent, the deformation capability of the members. It is noted that for the specimen with a wall thickness of 7 mm (AT7F0C), due to premature failure caused by out-of-plane instability during testing, its ductility data did not accurately reflect the positive effect of concrete filling.

Internal FRP reinforcement substantially improves ductility. Comparing the unreinforced specimen AT3F0C with the reinforced specimen AT3F4C, the displacement ductility ratio increased from 1.26 to 2.47—a rise of about 96%—and the energy absorption increased from 69.77 kN·mm to 714.32 kN·mm, representing a more than ninefold improvement. Similar trends were observed in specimens with wall thicknesses of 5 mm and 7 mm. This confirms that internal FRP reinforcement effectively enhances the overall ductility of GFRP–concrete composite arches, preventing brittle post-peak failure and promoting ductile behavior.

For unfilled hollow GFRP tube specimens, the displacement ductility ratio ranged between 1.17 and 1.33, indicating some deformation capacity. However, their energy absorption was significantly lower than that of corresponding filled specimens. This suggests that although hollow GFRP tubes exhibit limited ductility, their energy dissipation capacity remains low. After concrete filling and FRP reinforcement, the ductility performance transitioned from “limited deformation capacity” to “a well-developed ductile energy-dissipating mechanism.”

Based on the above analysis, incorporating internal FRP reinforcement is the most effective way to enhance the ductility of GFRP tube–concrete arches, while increasing the wall thickness of the GFRP tube can further improve their deformation and energy dissipation performance.

Load -strain curves

Fig.5 shows the load–longitudinal strain and load–hoop strain curves at the mid-span and quarter-span points. All specimens subjected to mid-span loading exhibited similar strain trends. Specimen series AT3F4C, AT3EC and AT3F0C were selected as representative examples for analyzing the longitudinal and hoop strains at different locations. Based on the strain response of the representative specimen AT3F4C at the mid-span and quarter-span points (Fig. 5), the failure process under mid-span concentrated load is clearly delineated: it initiated with flexural cracking of concrete, followed by significant internal force redistribution. In the initial linear-elastic stage, the longitudinal tensile strain at the mid-span bottom (Point 10) increased most rapidly, identifying it as the critical section. After the concrete cracked at approximately 10 kN, the longitudinal tensile strain stabilized, indicating a localized loss of flexural rigidity and the formation of a plastic hinge zone. This cracking triggered marked load redistribution, evidenced by the accelerated growth of both tensile strain at the quarter-span crowns (Points 2, 12) and compressive strain at their bottoms (Points 6, 16). This pattern confirms that bending moment increased substantially at the adjacent quarter-span sections after mid-span cracking. Concurrently, the hoop strain data, while consistently lower than longitudinal strains affirming a bending-dominated response, provide key evidence for an effective confinement mechanism. The persistent presence and development of hoop strains—such as tensile strains at the crowns (Points 1, 11) and tensile strains at the quarter-span bottoms (Points 5, 15)—demonstrate the GFRP tube's continuous resistance to concrete's lateral expansion. The development of these hoop strains correlates with the confinement mechanism. In conclusion, the strain evolution outlines a definitive process: flexural cracking triggers hinge formation and load redistribution. Given the primarily hoop-oriented fiber architecture (85°) of the GFRP tube, the ultimate capacity is governed by the tensile capacity of the longitudinal GFRP reinforcement in conjunction with the significant enhancement of compressive zone performance provided by the tube's hoop confinement. This confinement effect is substantiated by the progression of hoop strain and contributes crucially to the hinge's rotational capacity and the overall load-bearing capability.

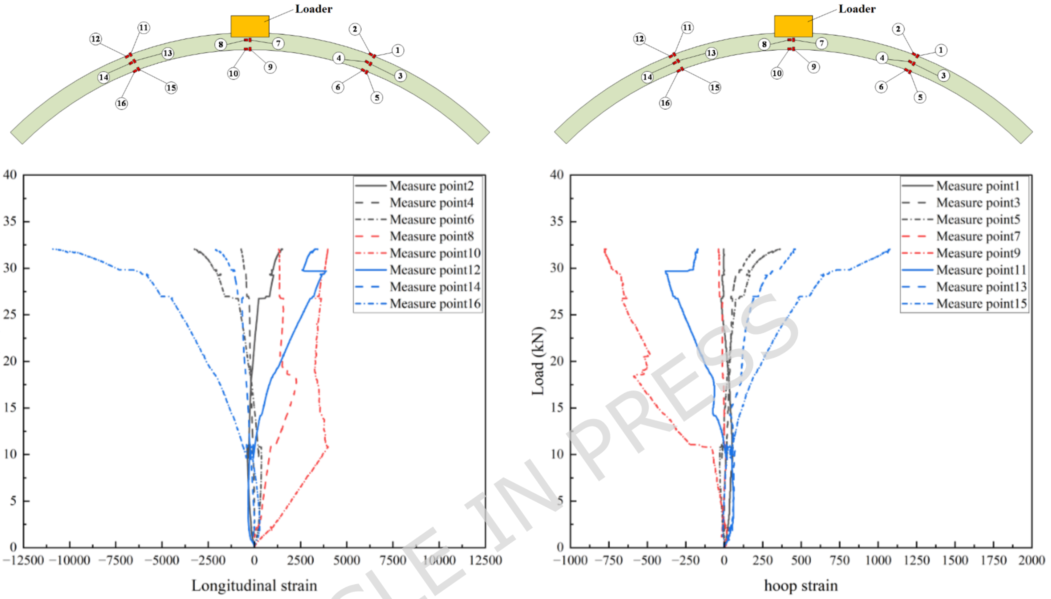

(a) Load-longitudinal strain curve of AT3F4C (b) Load-hoop strain curve of AT3F4C

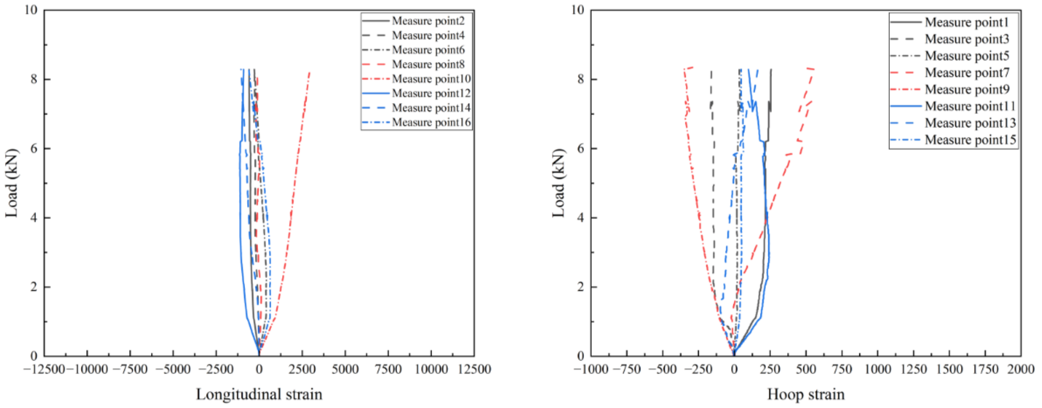

(c) Load-longitudinal strain curve of AT3EC (d) Load-hoop strain curve of AT3EC

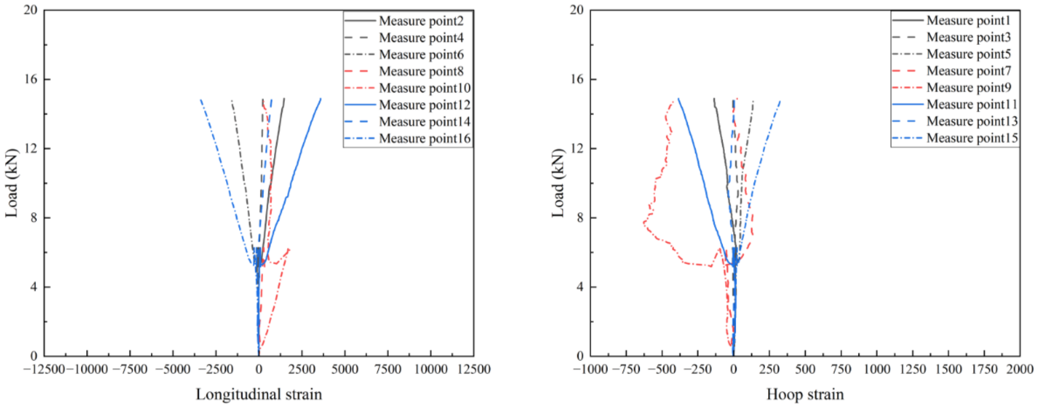

(e) Load-longitudinal strain curve of AT3F0C (f) Load-hoop strain curve of AT3F0C

Fig.5. Load-longitudinal strain curve and Load-hoop strain curve

Influence of boundary conditions

In the experiment, approximately ideal fixed boundaries were intended to be achieved through measures including supports with inclined surfaces matching the arch end sections, restraint by ring-shaped steel blocks, and filling of gaps with wooden wedges (as shown in Fig.3). Monitoring throughout the entire testing process confirmed that, within the measurement precision and applied load range, no displacement or rotation was observed at the supports, indicating that the actual rotational stiffness achieved at the supports was extremely high, meeting the design objective of a high degree of fixity. However, theoretically perfect, ideal fixity is challenging to achieve absolutely in experiments. Any unintended partial fixity may have nuanced effects on the results: Firstly, compared to a model with perfect fixity, actual slight flexibility at the supports would lead to a slight reduction in bending moment at the support and a corresponding slight increase in bending moment at the mid-span, resulting in a more uniform distribution of bending moment along the arch. Secondly, this may cause the measured initial stiffness to be slightly lower than the predicted values based on the assumption of perfect fixity. Finally, the sequence and locations of plastic hinge formation in the ultimate limit state might also change if rotation occurs at the support. These effects could be one of the potential reasons for the slight discrepancies between the analytical predictions and the experimental data.

Nevertheless, it is important to emphasize that this uncertainty in boundary conditions did not alter the core conclusion of this study regarding the improvement in ultimate bearing capacity due to the internal FRP bars. On the contrary, it demonstrates that the novel arch structure exhibits robust performance even with minor uncertainties in the boundary conditions. Subsequent research could employ more precise rotation sensors or design more complex loading schemes to directly quantify the actual rotational stiffness of the arch foot. Based on the above experimental observations and analysis, a perfectly fixed boundary condition will be adopted for modeling and comparative validation in the bearing capacity prediction model in the following section.

Bearing capacity prediction model

The composite arches in this study are fixed-ended arches without hinges, which are statically indeterminate to the third degree. For such an arch, the ultimate limit state is reached when four plastic hinges form in the structure, as illustrated in Fig. 6. Plastic hinge theory is adapted for these FRP-confined concrete composite arches. While FRP is linearly elastic, the confined concrete core exhibits a pronounced hardening response and significant deformation capacity under compression. Concurrently, the FRP reinforcement in tension undergoes large elastic deformation until rupture. This mechanical behavior allows the composite section to sustain a large increase in curvature without a loss of load capacity, thereby forming a “quasi-plastic” or “capacity” hinge. The experimental results presented also confirm that the fixed arch fails only after the development of four plastic hinges, which are typically located near the crown, both abutments, and randomly at one of the quarter-span points on the left or right side[24]. The observed load-displacement curves and strain histories from experiments, which demonstrate clear internal force redistribution prior to the peak load, provide direct evidence of this hinge-like mechanism. Therefore, once the bending moments at the four plastic hinge sections are determined, the ultimate load P of the arch can be derived using the principle of virtual work.

To analytically determine the moment capacity of the plastic hinges, the original circular composite section is transformed into an equivalent rectangular section. This transformation is analytically necessary to employ the well-established closed-form solutions for moment-curvature response available for rectangular sections. The equivalence is mechanically rigorous, established by enforcing two key properties to be identical[25]: (1) Equal Cross-Sectional Area, to preserve axial stiffness and mass properties critical for axial force-bending moment interaction; and (2) Equal Moment of Inertia, to ensure the flexural stiffness (EI) in the primary bending plane remains unchanged for accurate prediction of bending capacity and curvature. A circular section with radius r is thus converted into a rectangular section with dimensions $b \times h$. The dimensions are derived by solving the two equivalence conditions simultaneously, ensuring the essential load-resisting characteristics are preserved.

Furthermore, shear deformation effects are neglected in this analytical model. This assumption is justified for the specific configurations in this study. The arches possess a high rise-to-span ratio (0.206), and the section depth is relatively small compared to the span, classifying them as slender members where bending dominates. Critically, all experimental specimens failed due to FRP rupture at the crown or quarter-span points caused by excessive bending moment, with no observed shear-induced diagonal cracks or failures. Additionally, the FRP tube provides effective confinement that significantly enhances the member's shear capacity, making a shear-critical failure unlikely before the full development of flexural plastic hinges.

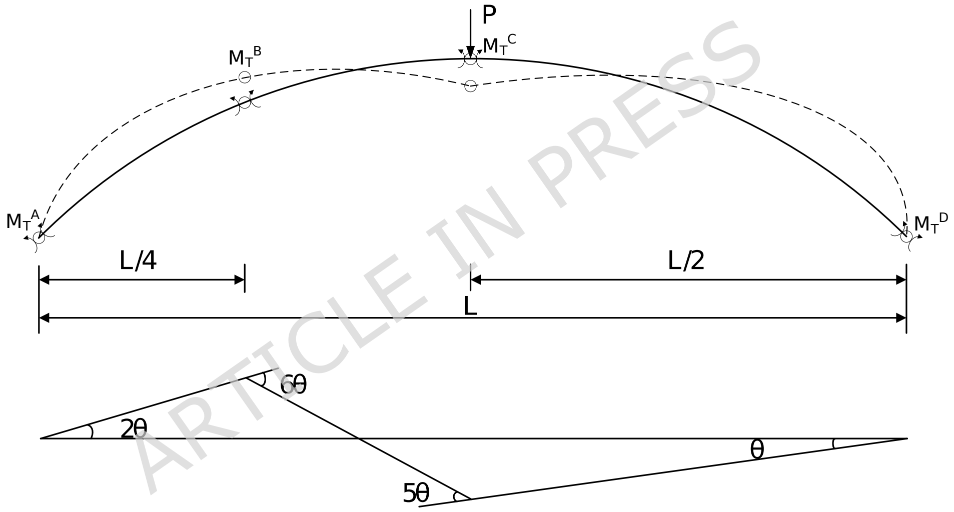

Fig. 6. Mechanism failure of arch under concentrated load at mid-span

Let M_T^i denote the ultimate bending moment at each plastic hinge, where the subscript i indicates its location. When a virtual displacement y is applied at the mid-span, the internal virtual work done by the moments V can be calculated by Eq. (1).

$$V = -\sum M_T^i \theta_i = -\left(2M_T^A + 6M_T^B + 5M_T^C + M_T^D\right)\theta \qquad (1)$$

where θ represents the virtual rotation angle. The external virtual work T done by the concentrated load P is calculated by Eq. (2) and Eq. (3).

$$\mathrm{V}y=\frac{1}{2}L\theta \tag{2}$$

$$T=P\times\mathrm{V}y=\frac{1}{2}PL\theta \tag{3}$$

According to the principle of virtual work: $V+T=0$，P can be calculated by Eq.(4).

$$P=\frac{2\left(2M_T^A+6M_T^B+5M_T^C+M_T^D\right)}{L} \tag{4}$$

A circular section with radius r can be equivalently converted into a rectangular section with dimensions $b\times h$ as analyzed above. The equivalence formulas are given as follows:

$$b=\frac{\pi}{\sqrt{3}}r, h=\sqrt{3}r \tag{5}$$

According to Eq. (5), the circular cross-section with radius r is transformed into an equivalent rectangular section of dimensions $b\times h$, resulting in the computational schematic of the concrete-filled composite tube arch section.

The sum of internal and external forces along the longitudinal axis of the member is zero, which is calculated by Eq. (6).

$$N_T=\alpha_1 f_{cc}bx-f_jA_{sj}-f_gh_gb \tag{6}$$

The sum of moments about the tensile GFRP reinforcement is zero. Therefore, M_T can be calculated by Eq. (7).

$$M_T = N_T e = \alpha_1 f_{cc} b \beta_1 x \left(h - \frac{x}{2} \right) - f_g h_g b \frac{h_g}{2} \tag{7}$$

Where x is the height of the concrete compression zone; f_j is the tensile strength of GFRP reinforcement under tension; h_g is the thickness of the composite tube; A_{sj} is the cross-sectional area of the tensile GFRP reinforcement; and f_g is the tensile strength of the composite tube; α_1 and β_1 are the reduction factors specified in the specification.

Lam and Teng[26,27] established a formula for calculating the confining stress based on the effective strain of FRP in their study, as shown in Eq. (8) and Eq. (9).

$$f_{cc} = f'_{c0} + \varphi_f \times K_1 \times f_l \tag{8}$$

$$f_l = \frac{2 E_{frp} \varepsilon_{frpu} t}{D} \tag{9}$$

Where f'_{c0} is the unconfined compressive strength of concrete; E_{frp} is the hoop elastic modulus of the FRP tube; ε_{frpu} is the ultimate tensile strain of the FRP tube; t is the wall thickness; D is the core concrete diameter; ψ_f is a reduction factor[28], taken as 0.95; and K_1 is the constraint efficiency coefficient, with a value of 3.3.

In accordance with code ACI 318-19 [29], the non-uniform stress distribution in the compression zone is simplified into an equivalent rectangular stress block for computational convenience. Since f'_{c0}

< 50 MPa, the following provisions apply: $\alpha_1=0.85$，$\beta_1=0.85$. The core of the ultimate analysis method lies in determining the ultimate moment of the cross-section. When calculating the ultimate bearing capacity of the concrete-filled composite tube arch, the N_T-M_T interaction diagram for the arch section is plotted based on Eq. (6) and Eq. (7). The relationship between the bending moment, axial force, and load P at each plastic hinge section of the arch is determined using the displacement method. By superimposing the axial force (N_P) - bending moment (M_P) interaction curve onto the section's N_T-M_T curve, the abscissa of their intersection point gives the ultimate moment value M_T^i for the section. Substituting M_T^i into Eq. (4) yields the ultimate bearing capacity P of the composite arch.

The predicted ultimate bearing capacities of the concrete-filled composite tube arches using this model for specimen AT3F4C, AT5F4C and AT7F4C are 31.28kN, 47.69kN and 63.56kN with their relative errors compared with experimental results equal to 2.4%, 10.4% and 9.1%, respectively. The error for the ultimate bearing capacity of the internally reinforced specimens is within 10%, indicating good accuracy of the theoretical calculation method.

It is noted that the above model is applicable to arches with a rise-to-span ratio within the tested range around 0.2 and a circular thin-walled FRP tube section. The FRP tube should have a primarily hoop-oriented layout, with normal concrete strength grades around C40 and internal longitudinal FRP bars. The model in its current form is validated only for in-plane symmetric loading under a single concentrated load at the crown with flexural failure. Its applicability to shear-dominated failures, local buckling, connection failures or other load patterns requires further verification.

Conclusion

This paper proposes a reinforced concrete-filled GFRP tubular arch suitable for underground engineering environments. Monotonic loading tests were conducted on eighteen arched specimens with different wall thicknesses (3 mm, 5 mm, 7 mm) and with or without embedded longitudinal GFRP reinforcement. Based on the experimental investigation, the following main conclusions are drawn:

(1) Increasing the wall thickness of the GFRP tube enhances the ultimate load-bearing capacity of the arch specimens. When compared to composite arch whose GFRP tube wall thickness is 3mm (specimen AT3F4C), specimens with wall thickness equal to 5mm and 7mm (specimens AT5F4C and AT7F4C) exhibits increases of 34.7% and 81.7% in ultimate load capacity, respectively.

(2) Embedding FRP reinforcement significantly improves the tensile resistance of the arches, and effectively increases the ultimate capacity and displacement ductility ratio of the arches under mid-span compression. Compared with hollow GFRP tubes, adding internal concrete leads to 62.7%~76.8% increase of ultimate capacity and 7.7%~35.3% increase of displacement ductility ratio. Further inserting GFRP bars brings 236.3%~279% increase of ultimate capacity and 111.11%-119.67% increase of displacement ductility ratio.

(3) The proposed theoretical model provides valid predictions for the ultimate load of concrete-filled FRP tubular arches. Comparisons between theoretical calculations and experimental results for three sets of reinforced specimens show that the error in ultimate load-bearing capacity is within 10%, verifying the accuracy of the method. It is important to highlight that the proposed plastic hinge model is currently validated only for the specific arch configuration presented in this study. While its theoretical framework is general, application to significantly different configurations requires additional validation or parametric study, which represents an important direction for future work.

The results demonstrate that concrete-filled GFRP tubular arches exhibit favorable load-carrying capacity and can serve as load-bearing and reinforcing elements in underground engineering applications.

Data availability statement

The data provided in the manuscript are comprehensive and available upon request to the corresponding author.

References

1. Liu, S. Y., Li, H. J., Tian, L. Y. et al. Some problems on polluted erosive durability of urban underground structures. *Chin. J. Geotech. Eng.* **38**, 7–11 (2016).

2. Lin, Q., Feng, C., Zhang, Y. et al. The failure evolution characteristic of the arched structure under blast loading. In Journal of Physics: Conference Series. 2535, 012020 (IOP Publishing, 2023).

3. Chen, H. L., Jin, F. N. & Fan, H. L. Elastic responses of underground circular arches considering dynamic soil-structure interaction: A theoretical analysis. *Acta Mech. Sinica-Prc* **29**, 110–122 (2013).

4. Aqoub, K., Mohamed, M. & Sheehan, T. Analysis of sequential

active and passive arching in granular soils. *Int. J. Geotech. Eng.* **15**, 598–607 (2021).

5. Ahmed, A. A. & Masmoudi, R. Axial response of concrete-filled FRP tube (CFFT) columns with internal bars. *J. Compos. Sci.* **2, 57** (2018).

6. Ostrowski, K., Dudek, M. & Sadowski, Ł. Compressive behaviour of concrete-filled carbon fiber-reinforced polymer steel composite tube columns made of high performance concrete. *Compos. Struct.* **234**, 111668 (2020).

7. Liao, J. J., Zeng J. J. , Zhuge, Y. et al. FRP-confined concrete columns with a stress reduction-recovery behavior: A state-of-the-art review, design recommendations and model assessments. *Compos. Struct.*, **321**, 117313 (2023).

8. Xia, Z. Y., Jiang, T. & Yu, T. Innovating arch structures with fiber-reinforced polymer composites: A review. *Adv. Struct. Eng.* **26**, 2341–2358 (2023).

9. Liao, J. J. , Zheng, Y. , Hu, S. W. et al. Behavior of concrete voussoir flexible arch bridges reinforced with FRP composites. *Eng. Struct.,* **312**,118229 (2024).

10. Dagher, H. J., Bannon, D. J., Davids, W. G. et al. Bending

behavior of concrete-filled tubular FRP arches for bridge structures. *Constr. Build. Mater.* **37**, 432–439 (2012)

11. Majeed, H. S., Davids, W. G. & Walton, H. J. Efficient second-order nonlinear finite-element simulation of concrete-filled FRP tubular arches. Structures **34**, 3738–3749 (2021).

12. Wang, H., Chen, H., Zhou, Y. et al. Blast responses and damage evaluation of CFRP tubular arches. *Constr. Build. Mater.* **196**, 233–244 (2019).

13. Liu, Y., Wang, H., Kong, X. et al. Static and Dynamic Performances of Concrete-Filled Braided CFRP Tubular Protective Structures. *J. Adv. Concr. Technol.* **18**, 532–544 (2020).

14. Dong, Z., Han, T., Zhang, B. et al. A review of the research and application progress of new types of concrete-filled FRP tubular members. *Constr. Build. Mater.* **312**, (2021).

15. Dong, Z., Liu, Z., Wu, G. et al. Study on mechanical properties of seawater sea-sand coral aggregate concrete-filled BFRP tubular arches. *Adv. Struct. Eng.* **25**, 1851–1865 (2022).

16. Wei, C., Liu, C., Hu, Q. et al. In-plane behaviors of FRP confined

concrete-filled steel tubular arches under mid-span concentrated loads. Structures **68**, (2024).

17. Burnton, P., McDonnell, D. & Fernando, D. Design and Construction of a Hybrid Double–Skin Tubular Arch Bridge. In Australian Small Bridges Conference, 9th, 2019, Surfers Paradise, Queensland, Australia. (2019).

18. Fernando, D., De Waal, L., Jiang, S. et al. Structural Behavior of Hybrid FRP–Concrete–Steel Double-Skin Tubular Arches: Experiments and Numerical Modeling. *J. Compos. Constr.* **28**, 04024054 (2024).

19. ASTM International. *Standard Test Method for Apparent Hoop Tensile Strength of Plastic or Reinforced Plastic Pipe by Split Disk Method* ASTM D2290-12. (West Conshohocken, PA, 2012).

20. Bi, J. Study on Behavior of the MCSCFC Tunnel Lining Segment Under Uniform Compression. Coal Science Research Institute (2023).

21. Sapozhnikov, S. B., Yu, S. M.., & Shanygin, A. N. Measurement of Hoop Strength in Wound Composite Ring Specimen Using Modified Split Disk Test. *Mech. Compos. Mater.***59**,77-88, (2023).

22. Standardization Administration of China. *Test Method for*

Compressive Properties of Fiber Reinforced Plastics GB/T 1448-2005. (China Standard Press, Beijing, 2005).

23. Ministry of Housing and Urban Rural Development of the People\'s Republic of China. *Standard Test Method for Physical and Mechanical Properties of Concrete* GB/T 50081-2019. (China Architecture & Building Press, Beijing, 2019).

24. Wu, M. Ultimate load of arch. *J. Chongqing Jiaotong Univ.* **(04)**, 36–45 (1983).

25. Xiao, W. & Tian, H. The Discussion of the Calculation Methods of Bearing Capacity of Normal Section of R.C. Eccentric Compression Member with Circular Section. *Sci. Technol. Eng.* **10**, 8878–8882 (2010).

26. Lam, L. & Teng, J. G. Design-oriented stress–strain model for FRP-confined concrete. *Constr. Build. Mater.* **17**, 471–489 (2003).

27. Lam, L. & Teng, J. G. Design-oriented stress-strain model for FRP-confined concrete in rectangular columns. *J. Reinf. Plast. Comp.* **22**, 1149–1186 (2003).

28. American Concrete Institute. *Guide for the Design and Construction of Externally Bonded FRP Systems for*

Strengthening Concrete Structures ACI 440.2R-17. (Farmington Hills, MI, 2017).

29. American Concrete Institute. *Building Code Requirements for Structural Concrete and Commentary* ACI 318-19. (Farmington Hills, MI, 2019).

Funding

The work was fully supported by the National Key Research and Development Program of China (Grant No. 2023YFB3711600) and the National Natural Science Foundation of China (Grant No. 52208252).

Author contributions

Benben Li: Writing- original draft, Conceptualization. Zhenyuan Yang: Formal analysis, Data curation. Yujun Qi: Funding acquisition, Writing- review & editing, Supervision. Zhenglong Zhou: Supervision. Guowei Wang: Formal analysis, Data curation.

Declarations

Competing interests

The authors declare no competing interests.

Additional information

Correspondence and requests for materials should be addressed to Y.J.Q.

Figure legends

Fig. 1. Manufacturing process of GFRP arches

Fig.2. Preparation of concrete-filled FRP tubular arches

Fig.3. The single-point mid-span loading testing

Fig.4. Failure modes and load-displacement curve of specimens

Fig.5. Load-longitudinal strain curve and Load-hoop strain curve

Fig. 6. Mechanism failure of arch under concentrated load at mid-span